A spectacular galactic scale magnetohydrodynamic powered wind in ESO 320-G030

(article starts on next page)

Astronomy & Astrophysics

LETTER TO THE EDITOR

A spectacular galactic scale magnetohydrodynamic powered wind in ESO 320-G030

M. D. Gorski[1,22], S. Aalto[1], S. König[1], C. F. Wethers[1], C. Yang[1], S. Muller[1], K. Onishi[1,7], M. Sato[1],
N. Falstad[1], J. G. Mangum[2], S. T. Linden[3], F. Combes[4], S. Martín[5,6], M. Imanishi[7], K. Wada[8],
L. Barcos-Muñoz[2,9], F. Stanley[10], S. García-Burillo[11], P. P. van der Werf[12], A. S. Evans[2,9], C. Henkel[13,15,14],
S. Viti[12,16], N. Harada[7,17], T. Díaz-Santos[18,19], J. S. Gallagher[20], and E. González-Alfonso[21]

1 Department of Space, Earth and Environment, Chalmers University of Technology, Onsala Space Observatory, 439 92 Onsala, Sweden
2 National Radio Astronomy Observatory, 520 Edgemont Road, Charlottesville, VA 22903-2475, USA
3 Department of Astronomy, University of Massachusetts at Amherst, Amherst, MA 01003, USA
4 Observatoire de Paris, LERMA, Collège de France, PSL University, CNRS, Sorbonne University, 75014 Paris, France
5 European Southern Observatory, Alonso de Córdova, 3107, Vitacura, Santiago 763-0355, Chile
6 Joint ALMA Observatory, Alonso de Córdova, 3107, Vitacura, Santiago 763-0355, Chile
7 National Astronomical Observatory of Japan, 2-21-1, Osawa, Mitaka, Tokyo 181-8588, Japan
8 Kagoshima University, 1-21-35, Kagoshima 890-0065, Japan
9 Department of Astronomy, University of Virginia, 530 McCormick Road, Charlottesville, VA 22903, USA
10 Institut de Radioastronomie Millimétrique (IRAM), 300 Rue de la Piscine, 38400 Saint-Martin-d'Hères, France
11 Observatorio Astronómico Nacional (OAN-IGN), Observatorio de Madrid, Alfonso XII, 3, 28014 Madrid, Spain
12 Leiden Observatory, Leiden University, PO Box 9513, 2300 RA Leiden, The Netherlands
13 Max-Planck-Institut für Radioastronomie, Auf-dem-Hügel 69, 53121 Bonn, Germany
14 Xinjiang Astronomical Observatory, Chinese Academy of Sciences, 830011 Urumqi, PR China
15 Astron. Dept., Faculty of Science, King Abdulaziz University, PO Box 80203, Jeddah 21589, Saudi Arabia
16 Department of Physics and Astronomy, University College London, Gower Street, London WC1E 6BT, UK
17 Astronomical Science Program, Graduate Institute for Advanced Studies, SOKENDAI, 2-21-1 Osawa, Mitaka, Tokyo 181-1855, Japan
18 Institute of Astrophysics, Foundation for Research and Technology-Hellas (FORTH), Heraklion 70013, Greece
19 School of Sciences, European University Cyprus, Diogenes street, Engomi 1516 Nicosia, Cyprus
20 Department of Astronomy, University of Wisconsin, 475 North Charter St., Madison, WI 53706, USA
21 Universidad de Alcalá, Departamento de Física y Matemáticas, Campus Universitario, 28871 Alcalá de Henares, Madrid, Spain
22 Center for Interdisciplinary Exploration and Research in Astrophysics (CIERA) and Department of Physics and Astronomy, Northwestern University, Evanston, IL 60208, USA
   e-mail: mark.gorski@northwestern.edu

ABSTRACT

How galaxies regulate nuclear growth through gas accretion by supermassive black holes (SMBHs) is one of the most fundamental questions in galaxy evolution. One potential way to regulate nuclear growth is through a galactic wind that removes gas from the nucleus. It is unclear whether galactic winds are powered by jets, mechanical winds, radiation, or via magnetohydrodynamic (MHD) processes. Compact obscured nuclei represent a significant phase of galactic nuclear growth. These galaxies hide growing SMBHs or unusual starbursts in their very opaque, extremely compact ($r < 100\,\mathrm{pc}$) centres. They are found in approximately 30% of the luminous and ultra-luminous infrared galaxy population. Here, we present high-resolution ALMA observations ($\sim$30 mas, $\sim$5 pc) of ground-state and vibrationally excited HCN towards ESO 320-G030 (IRAS 11506-3851). ESO 320-G030 is an isolated luminous infrared galaxy known to host a compact obscured nucleus and a kiloparsec-scale molecular wind. Our analysis of these high-resolution observations excludes the possibility of a starburst-driven wind, a mechanically or energy driven active galactic nucleus wind, and exposes a molecular MDH wind. These results imply that the nuclear evolution of galaxies and the growth of SMBHs are similar to the growth of hot cores or protostars where gravitational collapse of the nuclear torus drives a MHD wind. These results mean galaxies are capable, in part, of regulating the evolution of their nuclei without feedback.

Key words. galaxies: evolution – galaxies: ISM – galaxies: clusters: individual: ESO 320-G030 – galaxies: nuclei – galaxies: structure

1. Introduction

A fundamental process in galaxy evolution is supermassive black hole (SMBH) growth (e.g., Sanders & Mirabel 1996; Ferrarese & Merritt 2000; Fabian 2012). One potential way to regulate nuclear growth is through feedback. Energy and momentum injected into the interstellar medium (ISM) from intense episodes of star formation (e.g., Lehnert et al.

1999; Leroy et al. 2018; Bolatto et al. 2021) and active galactic nuclei (AGNs; e.g., García-Burillo et al. 2014) can hinder nuclear growth by removing gas in the form of galactic winds, which are commonly observed in galaxies (Veilleux et al. 2020). Astronomers currently debate whether AGN-driven galactic outflows are fuelled by jets, mechanical winds, or radiation (Faucher-Giguère & Quataert 2012; Wada 2012; Costa et al. 2014; Veilleux et al. 2020; Ishibashi et al. 2021). Magnetohydrodynamic (MHD) winds, which are not the result of feedback, could also regulate nuclear growth (e.g., Chan & Krolik 2017; Vollmer et al. 2018; Girichidis et al. 2018; Takasao et al. 2022), as suggested by Aalto et al. (2020) within the galaxy NGC 1377. MHD winds remove material from the nucleus, but also allow for accretion onto a central object by removing angular momentum from the system (Blandford & Payne 1982; Ray & Ferreira 2021). Although radio jets are a MHD phenomenon that may entrain molecular gas (e.g., Morganti et al. 2007), molecular MHD winds are a less widely accepted explanation for the mechanism behind galactic winds.

Hiding either growing SMBHs or unusual starbursts, compact obscured nuclei (CONs) represent a key phase of galactic nuclear evolution (Aalto et al. 2015b). The most intense phase of SMBH growth is theorized to occur when it is profoundly dust enshrouded (Hickox & Alexander 2018, and references therein). CONs are galaxy nuclei that are compact ($r < 100$ pc), hot ($T > 100$ K), and opaque ($N(H_2) > 10^{24}$ cm^{-2}), and identified by a luminosity surface density of the vibrationally excited HCN $v2 = 1f$ $J = 3-2$ (HCN-vib) transition (rest frequency 265.85270940 GHz) greater than $1 L_\odot$ pc^{-2}. It is established that about ~40% of ultra-luminous infrared galaxies (ULIRGs) and ~20% of luminous infrared galaxies (LIRGs) contain CONs within the nearby universe ($D_L \lesssim 100$ Mpc, Falstad et al. 2021). CON nuclei are thought to be almost completely opaque with extinctions of $A_v > 1000$ (e.g., Treister et al. 2010; Roche et al. 2015). These galaxies provide an opportunity for us to investigate the correlations between the nuclear growth processes in galaxies, SMBHs, and global galaxy characteristics.

Falstad et al. (2021) identified ESO 320-G030 (IRAS F11506-3851) as a host to a CON with a HCN-vib luminosity of $1.4 \pm 0.2 L_\odot$ pc^{-2}. ESO 320-G030 is an isolated LIRG (Sanders et al. 2003), with regular rotation (Bellocchi et al. 2013), a double-barred structure (Greusard et al. 2000), and no signs of a recent interaction (Arribas et al. 2008). It has a luminosity distance of 36 Mpc ($z = 0.0103$) (Sanders et al. 2003) using a flat cosmology with $H_0 = 75$ km s^{-1} Mpc^{-1}, $\Omega_M = 0.3$, and $\Omega_\Lambda = 0.7$. The systemic velocity is ~3080 km s^{-1} (Pereira-Santaella et al. 2016) and it has an infrared luminosity of ~10^{11} $L_\odot$ (Sanders et al. 2003). It lacks traditional indications of an AGN based on X-ray or mid-infrared observations (Pereira-Santaella et al. 2010, 2011), and it lacks the flat radio spectrum of a radio-loud AGN (Baan & Klöckner 2006) to power its OH megamaser (Staveley-Smith et al. 1992). The galaxy harbours a multiphase outflow observed from 100 pc to kiloparsec scales (e.g., Arribas et al. 2014; Cazzoli et al. 2014; Pereira-Santaella et al. 2016, 2020), but the source of this outflow is claimed to be within the innermost 250 pc of the galaxy's nucleus (Pereira-Santaella et al. 2020).

In this work we present high-resolution (~30 mas, ~5 pc) Atacama Large Millimeter/Submillimeter Array (ALMA) observations of ESO 320-G030. Due to the proximity of ESO 320-G030, and the high quality of the ALMA data, we are able to reveal the launching region of the molecular outflow. We present the properties of the observations in Sect. 2, and the observed properties of both ground-state and vibrationally excited HCN transitions as well as the continuum emission in Sect. 3. In Sect. 4 we discuss the nuclear – and outflow – properties of ESO 320-G030. Our findings on the wind origin are summarized in Sect. 5.

2. Observations

Our ALMA observations are part of the CONfirm project (PI Falstad, N., project code 2019.1.01612.S) which contain the HCN $v = 0$, $J = 3-2$ (rest frequency 265.8864343 GHz) and HCN $v2 = 1f$, $J = 3-2$ transitions (hereafter HCN-vib, rest frequency 267.19928300 GHz) towards ESO 320-G030. We combine three scheduling blocks, two from September 6, 2021, and one from September 28, 2021. The three scheduling blocks utilized 42, 42, and 44 antennas, respectively. The respective average precipitable water vapour was ~2.1 mm, ~2.2 mm, and ~0.7 mm. The longest baseline was 16.2 km corresponding to the highest possible angular resolution of 20 mas at 260 GHz. The fifth percentile baseline length corresponds to a maximum recoverable scale of 0.″4.

The calibration of and imaging of the data were done in CASA (CASA Team 2022). The spectral setup consists of two 1.875 GHz spectral windows containing 240 channels centred at 265.005 GHz and 263.182 GHz. Two additional 2.000 GHz spectral windows with 128 channels are centred at 248.447 GHz and 250.427 GHz. The original synthesized beam is 30.9 mas × 28.8 mas with a natural weighting of the visibilities. The final image cubes have 18 MHz wide (~20 km s^{-1}) channels imaged to a common beam of 31 mas × 31 mas (5.3 pc × 5.3 pc at a distance of 36 Mpc) with 6.5 mas pixels, resulting in a root-mean-square (rms) of 0.22 mJy beam^{-1}.

3. Results

3.1. Continuum

We have combined the two 2.0 GHz spectral windows and the line-free channels from the 1.875 GHz spectral windows to generate a 256 GHz continuum image (Fig. 1) with a rms of 21 μJy beam^{-1}. A two-dimensional Gaussian fit to the continuum emission, masking pixels below 80% of the peak intensity, reveals a central deconvolved source with a full width at half maximum (FWHM) of 68.2 ± 0.8 mas by 30.5 ± 0.4 mas at a position angle of $120.8 \pm 0.5°$. At a distance of 36 Mpc, the physical size is 11.9×5.3 pc, that is, of a similar size to nearby dusty AGN tori (Combes et al. 2019; García-Burillo et al. 2021).

3.2. HCN emission

We used the STATCONT software package (Sánchez-Monge et al. 2018) to perform the continuum subtraction on the image cubes. STATCONT statistically derives the continuum on a pixel-by-pixel basis. We utilized the sigma clipping method and specify a rms of 0.22 mJy beam^{-1} per channel.

Both the vibrational ground and first excited states of HCN 3−2 have been detected towards ESO 320-G030. Ground-state HCN 3−2 emission is observed in a ~0.″5 (87 pc) structure, whereas the excited vibrational state (HCN-vib) is only detected in the innermost 80 mas (14 pc; Fig. 1). Figures 2 and 3 show the respective integrated intensity and intensity-weighted velocity maps of the ground-state HCN $J = 3-2$ line. The intensity-weighted velocity maps only include pixels >3× rms of the data cube. The ground-state line is generally seen in emission, though
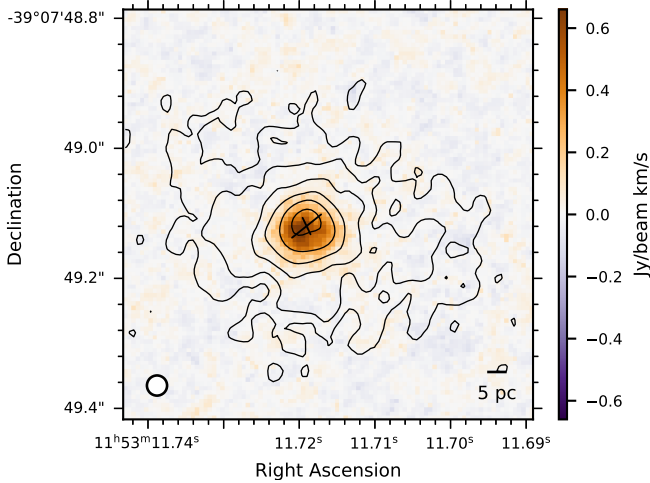
Fig. 1. Integrated flux map of the vibrationally excited HCN $v2 = 1f$, $J = 3-2$ transition. The contours show the 256 GHz continuum with levels at $0.02 \times (3, 6, 12, 24, 48, \text{and } 96)$ mJy beam^{-1}. The cross indicates the position and orientation of the 68.2 mas by 30.5 mas Gaussian fit to the continuum peak.
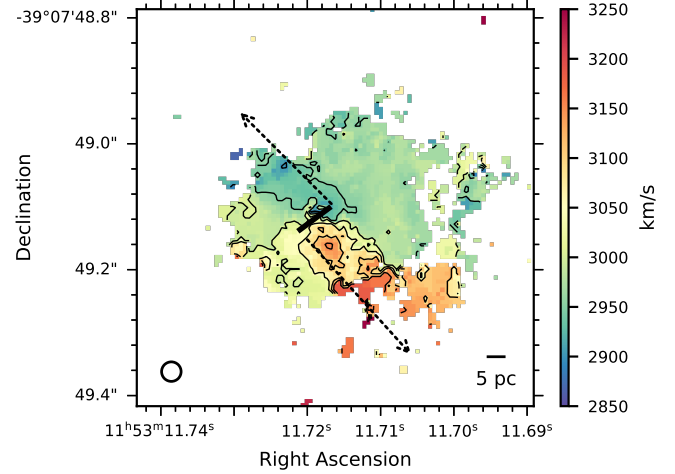

Fig. 3. Intensity-weighted velocity map (moment 1) of the ground-state HCN $J = 3-2$ transition. The contours range from 2850 km s^{-1} to 3250 km s^{-1} with steps of 50 km s^{-1}. The black line indicates the major axis of the two-dimensional Gaussian fit to the peak intensity of the continuum. The rough location and direction of the outflow (this work) is indicated by the dashed arrows.
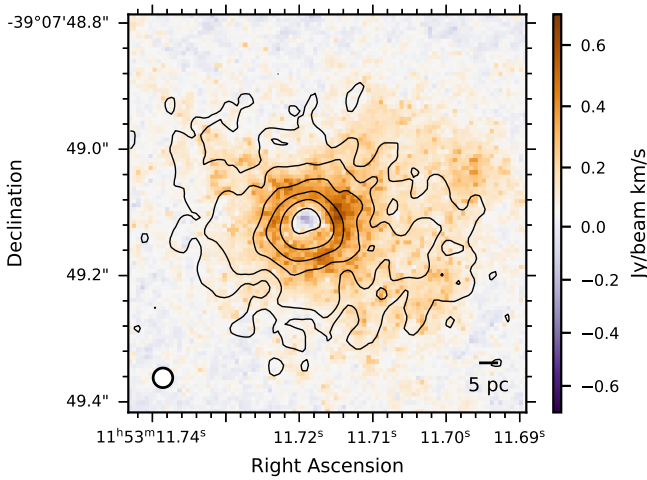

Fig. 2. Integrated flux map (moment 0) of the ground-state HCN $J = 3-2$ transition. The contour levels are $0.039 \times (4, 8, 16, \text{and } 32)$ Jy beam^{-1} km s^{-1}.

Fig. 4. Intensity-weighted velocity field (moment 1) of the vibrationally excited HCN-vib transition, showing the base of the outflow. The black line indicates the major axis of the two-dimensional Gaussian fit to the peak intensity of the continuum. The rough location and direction of the outflow is indicated by the dashed arrows. Rotation is seen along the major axis of the continuum, with the blueshifted side to the northwest. The red and blue contours are integrated flux maps of $|v| > 100$ km s^{-1} HCN-vib emission with levels at three and eight times 0.012 Jy km s^{-1}. These contours show that the HCN-vib emission is extended along the outflow, and that the outflow is launched from similarly rotating sides of the nucleus.

it can be seen in absorption towards the peak of the continuum (Fig. 2).

The ground-state HCN intensity-weighted velocity map indicates a two-sided outflow, with the blueshifted lobe proceeding to the northeast and the redshifted lobe proceeding to the southwest. The outflow has observed velocities >100 km s^{-1} in both directions (Fig. 3). The HCN-vib intensity-weighted velocity map (Fig. 4) shows rotation in the centremost 20 pc.

3.3. Vibrational HCN morphology

The rotational transitions of vibrationally excited HCN occur in the $v_2 = 1$ state, which has an energy above the ground state of 1024 K. A critical density of $\sim 10^{11}$ cm^{-3} is necessary to collisionally excite these transitions (Ziurys & Turner 1986), making HCN-vib emission a viable probe of the opaque nuclei of galaxies (e.g., Martín et al. 2016). The high critical density likely means that radiative excitation populates the vibrationally
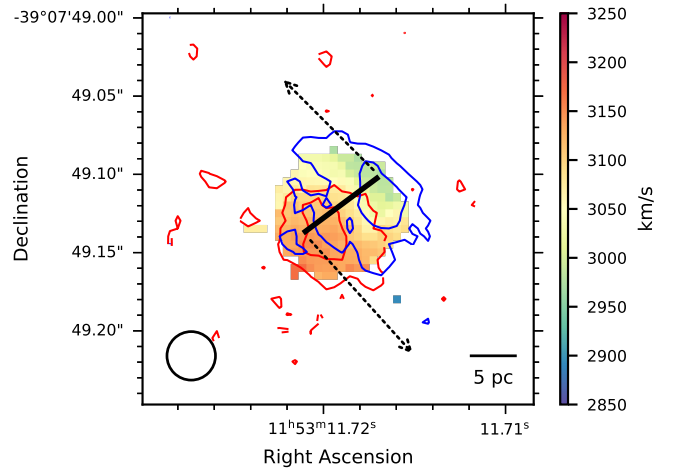
excited states. Aalto et al. (2015a) claim HCN-vib can directly trace the structure and dynamics of optically thick dust cores.

The HCN-vib traces a compact region about the nucleus approximately 80 mas (14 pc) in diameter. The velocity field shows rotation with a projected velocity of roughly 100 km s^{-1}. Integrated flux maps ($|v| > 100$ km s^{-1} with respect to the systemic velocity) indicate that emission is extended along the axis of the molecular outflow (Fig. 4).
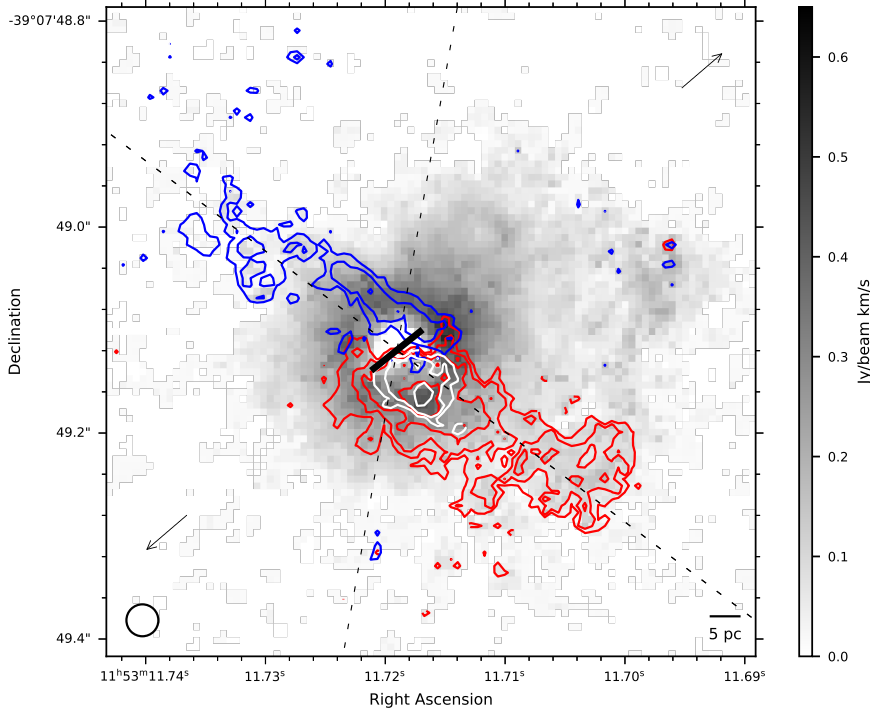
Fig. 5. Integrated ground-state HCN $\nu = 0$ $J = 3-2$ emission (gray scale), with $|v| > 100\,\mathrm{km\,s^{-1}}$ (with respect to the systemic velocity) contours at $0.015 \times (3,\ 5,\ 8,\ \mathrm{and}\ 13)\ \mathrm{Jy\,km\,s^{-1}}$. The blue contours show the approaching outflow, and the red contours show the receding outflow. The white contours show the $v > 200\,\mathrm{km\,s^{-1}}$ gas. The black line indicates the major axis of the two-dimensional Gaussian fit to the peak intensity of the continuum. The dashed black line indicates the orientation of the outflow indicated by Pereira-Santaella et al. (2016, 2020), and the arrows indicate the tentative direction of a radio elongation from Hekatelyne et al. (2020).

4. Discussion

4.1. Outflow morphology

To image the outflow, we created two HCN 3–2 integrated flux maps. We included channels that, by eye, are dominated by the outflow $|v - v_{\mathrm{sys}}| > 100\,\mathrm{km\,s^{-1}}$ (Fig. 5). We observed the outflow out to $0\rlap{.}''3$ (52 pc) in HCN 3–2. We also applied a Hanning kernel data cube, degrading the spectral resolution to 36 MHz ($\sim$40 km s^{-1}) and thus improving the rms to 0.14 mJy beam^{-1}. Figure 6 shows five individual channels of the ground-state HCN line.

In Fig. 5 the black bar shows the orientation of the nuclear region for reference, and the base of the outflow is seen separated by the approximate width of the continuum. There exists a velocity shift along the major axis of the continuum that is consistent with the rotation observed in the HCN-vib line. The velocity shift in the outflow is approximately $\pm 150\,\mathrm{km\,s^{-1}}$ (projected). The gas is roughly consistent with the 200 pc to kiloparsec scale outflow observed by Pereira-Santaella et al. (2016, 2020) with position angles between $-10°$ and $53°$ (Fig. 5) and with velocities of $|v| < 300\,\mathrm{km\,s^{-1}}$.

What is spectacular about the outflow morphology is that the launching regions are apparent and connected to the rotating nuclear structure in the innermost $\sim$12 pc. The launch region of the blueshifted lobe is clearly separated from the redshifted lobe. Additionally, in Fig. 6 the blue contours (3124 km s^{-1}) indicate the approaching side of the redshifted lobe and the red contours (3163 km s^{-1}) show the receding side of the redshifted lobe. There is a clear east-west shift in the redshifted lobe, indicative of rotation in the outflow (see Fig. 12 from Aalto et al. 2020). The 3242 km s^{-1} contours (white) also show evidence of a highly inclined disk, suggesting the inclination derived from the continuum is accurate or a lower limit. The flux density drops from $\sim$7σ to zero within one beam, forming a straight line consistent with an almost edge-on, or near edge-on, disk.

To estimate the molecular mass of the outflow, we measured the integrated flux in the maps of the outflowing gas. We

first converted the HCN $J = 3-2$ line luminosity to HCN 1–0, assuming a line ratio of 0.5 as in Aalto et al. (2015a). With this, we utilized the L(HCN)-to-H$_2$ conversion factor, calibrated for HCN $J = 1-0$ (Gao & Solomon 2004), and modified for ULIRGs and HCN-bright environments by García-Burillo et al. (2012). The conversion is $M_{\mathrm{dense}} \approx 3.1\,M_\odot/L'^{-1} \times L(\mathrm{HCN}\,1-0)$, where the units on L' are K km s^{-1} pc^{-2}. We measured a total HCN $J = 3-2$ luminosity from the blue and red outflows of $3.4 \pm 0.1 \times 10^6$ K km s^{-1} pc^{-2}, and obtained an outflow mass of $2.1 \times 10^7\,M_\odot$ within a radius of 52 pc. The mass is a lower limit as only the higher velocity gas is included in the outflow maps, and portions of the blueshifted lobe are not included due to line-of-sight effects as discussed in Sect. 4.3.

4.2. Outflow momentum

We now explain how we estimated the mechanical luminosity of the outflow to attempt to understand the power source. Momentum-driven outflows may exceed L_{Edd}/c up to a factor of five (Roth et al. 2012), whereas energy-driven outflows may exceed $10 L_{\mathrm{Edd}}/c$ (Costa et al. 2014). Determining the mechanical luminosity of the molecular outflow is difficult due to substantial uncertainties on the molecular mass and inclination. The kinetic energy of the outflow is $E_{\mathrm{outflow}} = (0.5 M_{\mathrm{out}} \times V_{\mathrm{out}}^2) + E_{\mathrm{turb}}$ (Veilleux et al. 2001). We assumed that turbulent kinetic energy is insignificant. We adopted the inclination derived from the axial ratio of the continuum of $63.4 \pm 0.5°$ and the outflow mass derived in the previous paragraph. For a projected velocity of 217 ± 14 km s^{-1}, taken from the average of the maximum observed velocities of the red (3322 km s^{-1}) and blue (2828 km s^{-1}) lobes and one channel width uncertainty, the outflow velocity is $V_{\mathrm{out}} = 515 \pm 33$ km s^{-1}. The total kinetic energy of the outflow is then $(6.5 \pm 0.8) \times 10^{55}$ erg. For a radial extent of the outflow of 52 pc, measured from the extent of the 3.3 Jy km s^{-1} ground-state HCN contour, this kinetic energy results in a mechanical luminosity of $(5.8 \pm 1.1) \times 10^9\,L_\odot$. It is
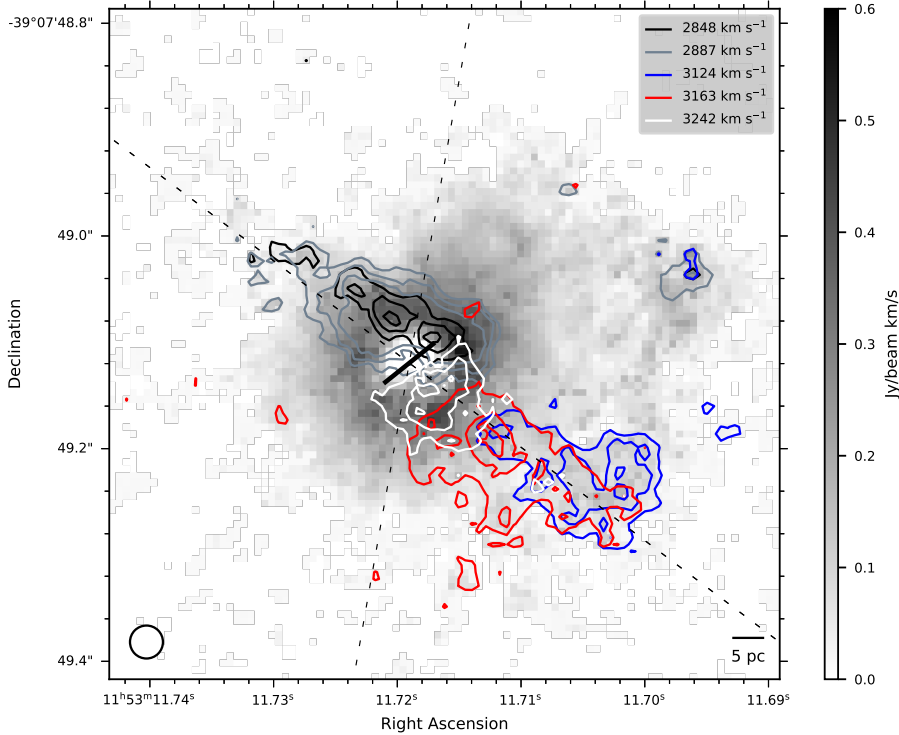
Fig. 6. Integrated ground-state HCN $v = 0$ $J = 3-2$ emission (gray scale), and 36 MHz ($\sim$40 km s^{-1}) wide channel maps with contours at $0.14 \times (5, 7, \text{and } 9)$ mJy. The blue contours show the approaching side of the redshifted lobe, and the red contours show the receding side of the redshifted lobe. The white contours show some of the highest velocity gas. Black and gray contours show the blueshifted lobe.

important to note that the following result is a lower limit to the outflow rate and momentum flux. The outflow rate and momentum flux are respectively $231 \pm 15\,M_\odot\,\text{yr}^{-1}$ and $(6.2 \pm 0.8) \times 10^{12}\,L_\odot/c$.

For ESO 320-G030, González-Alfonso et al. (2021) estimate the mass of the black hole, from the M_{BH}/σ relation, to be between $5 \times 10^6\,M_\odot$ and $8 \times 10^6\,M_\odot$. The corresponding Eddington luminosity is $2.1 \pm 0.5 \times 10^{11}\,L_\odot$. The momentum flux of the outflow is $30 \pm 7 \times L_{\text{Edd}}/c$ for a $6.5 \times 10^6\,M_\odot$ black hole. It is unlikely that the black hole is much larger than this, as the enclosed mass estimated from the HCN-vib emission within 70 mas (12 pc) and a rotation of 100 km s^{-1} is $7 \times 10^7\,M_\odot$. Furthermore, the outflow momentum flux exceeds the total infrared luminosity of the galaxy (L_{IR}/c) by a factor of 63 ± 8.

The analysis of the momentum flux reveals that the outflow is unlikely to be momentum driven by an AGN, as this exceeds the factor of five limit estimated by Roth et al. (2012). It is similarly unlikely to be star formation driven, since starburst-driven outflows appear to have a momentum limit of $1–3L_{\text{bol}}/c$ (Geach et al. 2014). In LIRGs, $L_{\text{bol}} \approx L_{\text{IR}}$ (Sanders & Mirabel 1996). Hence, even if all the star formation luminosity was emerging from the inner launch region of the outflow, the momentum flux is too high by a factor of ten. In addition, we know that only a small fraction of the star formation is contained within the nucleus, as revealed by Paα maps (Sánchez-García et al. 2022), so the infrared momentum flux of the entire galaxy acts as a conservative upper limit. The remaining possibilities are an energy-driven AGN wind (e.g., Faucher-Giguère & Quataert 2012; Costa et al. 2014), which is capable of powering momentum fluxes in excess of $10 \times L_{\text{Edd}}/c$, a radio jet, or a MHD-powered wind.

4.3. The outflow power source

It is difficult to ascertain which of the remaining mechanisms, from the previous section, dominate in ESO 320-G030. A radio-jet-powered outflow would technically be possible. ESO 320-G030 shows tentative evidence for a radio jet (Fig. 3 from Hekatelyne et al. 2020); however, it is incorrectly oriented to power the molecular outflow (Fig. 5). The radio extension is also not detected in the higher-resolution observations by Baan & Klöckner (2006).

A central constituent of an energy-driven AGN wind is a hot ionized component (Faucher-Giguère & Quataert 2012). The hot AGN wind entrains molecular gas in the torus, and the torus collimates the outflow (e.g., García-Burillo et al. 2019). Cazzoli et al. (2014) suggest that an ionized outflow is sometimes seen in the northeast of the ESO 320-G030. The detection is very tentative, and claimed to trace the outer edge of the wind. However, analysis by Bellocchi et al. (2013) and Pereira-Santaella et al. (2016) do not confirm the existence of an ionized outflow. The maximum ionized outflow velocity is estimated to be $\sim$100 km s^{-1} (Arribas et al. 2014). In addition, the X-ray, mid-infrared, optical, and radio spectra do not corroborate the existence of an AGN. ESO 320-G030's X-ray spectrum neither shows the Fe Kα line indicative of Compton-thick AGN (Pereira-Santaella et al. 2011), nor does the mid-infrared spectrum show the high ionization AGN lines [Ne V] 14.32 μm, [Ne V] 24.32 μm, or [O IV] 25.89 μm (Pereira-Santaella et al. 2010). [NII]/Hα and [OIII]/Hβ diagnostics also corroborate the lack of an AGN. ESO 320-G030 has a HII type spectrum (van den Broek et al. 1991; Pereira-Santaella et al. 2011), and it is missing the corresponding radio diagnostics of an AGN (Baan & Klöckner 2006). These are crucial missing components to an energy-driven AGN outflow.

The key lies in the morpho-kinematic structure. Figures 5 and 6 clearly reveal the imprint of nuclear rotation in the outflow. The redshifted and blueshifted lobes of the outflow appear to be launched from the respective rotating sides of the inner nuclear structure. The redshifted lobe also shows an east-west velocity shift (Fig. 6). There also appears to be a deficiency of material on the blueshifted lobe of the outflow compared with the redshifted

lobe and higher velocity gas near the nucleus. Furthermore, the outflow achieves a momentum flux exceeding $30 L_{Edd}/c$ within a radius of 100 pc. A $10^8 M_\odot$ black hole accreting at the Eddington accretion rate can produce a momentum flux of $\sim 26 L_{Edd}/c$, but this requires kiloparsec scales for the outflow to cool (Costa et al. 2014). As ESO 320-G030's outflow significantly exceeds the momentum flux upper limit for dusty radiation-driven outflows on 10∼100 pc scales, and since the SMBH mass cannot exceed the mass enclosed of $7 \times 10^7 M_\odot$, it is highly likely the dominant mechanism driving the outflow is not an energy-driven AGN. In the protostellar analogy proposed by Gorski et al. (2023), this makes sense in the context of a rotating infalling envelope and a MHD-powered outflow (e.g., Sakai et al. 2014; Oya et al. 2014, 2021). The lack of material is a line-of-sight effect where the redshifted side of the blueshifted lobe is confused with, or obscured by, the gas rotating closer to the systemic velocity of the galaxy. The outflow reappears once it emerges from the apparent extent of the envelope. The rotation of outflows is a strong indication of magnetic acceleration (Bjerkeli et al. 2016; Proga 2007, and references therein). Pudritz & Banerjee (2005) concluded that jets and outflows are inherent to the collapse of magnetized cores, and their properties are independent of the system's mass. Here, the outflow emerges from the centre of a rotating disk with a significant amount of angular momentum indicative of a MHD wind.

5. Conclusion

The astronomical community actively debates whether galactic outflows are driven by jets, mechanical winds, or radiation. In this Letter, we present compelling evidence that the outflow in ESO 320-G030 is powered by a different mechanism, a MHD wind launched prior to the ignition of an AGN. The overall morpho-kinematic structure appears to be consistent with a rotating disk and a rotating outflow. Analysis of the momentum flux excludes mechanically driven AGN, energy-driven AGN, or starburst-driven winds. The lack of an ionized outflow, or corresponding X-ray, radio, infrared, or optical counterparts suggests that there is no AGN or very weak AGN incapable of powering the outflow. What remains is a MHD wind, as evidenced by the rotating outflow. These results paint the following picture: that the nuclear evolution of galaxies and the growth of SMBHs is analogous to the growth of hot cores or protostars; feedback may not be necessary to drive a galactic wind; and nuclear evolution is regulated, at least in part, by MHD processes.

References

Aalto, S., Garcia-Burillo, S., Muller, S., et al. 2015a, A&A, 574, A85
Aalto, S., Martín, S., Costagliola, F., et al. 2015b, A&A, 584, A42
Aalto, S., Falstad, N., Muller, S., et al. 2020, A&A, 640, A104
Arribas, S., Colina, L., Monreal-Ibero, A., et al. 2008, A&A, 479, 687
Arribas, S., Colina, L., Bellocchi, E., Maiolino, R., & Villar-Martín, M. 2014, A&A, 568, A14
Baan, W. A., & Klöckner, H. R. 2006, A&A, 449, 559
Bellocchi, E., Arribas, S., Colina, L., & Miralles-Caballero, D. 2013, A&A, 557, A59
Bjerkeli, P., van der Wiel, M. H. D., Harsono, D., Ramsey, J. P., & Jørgensen, J. K. 2016, Nature, 540, 406
Blandford, R. D., & Payne, D. G. 1982, MNRAS, 199, 883
Bolatto, A. D., Leroy, A. K., Levy, R. C., et al. 2021, ApJ, 923, 83
CASA Team (Bean, B., et al.) 2022, PASP, 134, 114501
Cazzoli, S., Arribas, S., Colina, L., et al. 2014, A&A, 569, A14
Chan, C.-H., & Krolik, J. H. 2017, ApJ, 843, 58
Combes, F., García-Burillo, S., Audibert, A., et al. 2019, A&A, 623, A79
Costa, T., Sijacki, D., & Haehnelt, M. G. 2014, MNRAS, 444, 2355
Fabian, A. C. 2012, ARA&A, 50, 455
Falstad, N., Aalto, S., König, S., et al. 2021, A&A, 649, A105
Faucher-Giguère, C.-A., & Quataert, E. 2012, MNRAS, 425, 605
Ferrarese, L., & Merritt, D. 2000, ApJ, 539, L9
Gao, Y., & Solomon, P. M. 2004, ApJ, 606, 271
García-Burillo, S., Usero, A., Alonso-Herrero, A., et al. 2012, A&A, 539, A8
García-Burillo, S., Combes, F., Usero, A., et al. 2014, A&A, 567, A125
García-Burillo, S., Combes, F., Ramos Almeida, C., et al. 2019, A&A, 632, A61
García-Burillo, S., Alonso-Herrero, A., Ramos Almeida, C., et al. 2021, A&A, 652, A98
Geach, J. E., Hickox, R. C., Diamond-Stanic, A. M., et al. 2014, Nature, 516, 68
Girichidis, P., Naab, T., Hanasz, M., & Walch, S. 2018, MNRAS, 479, 3042
González-Alfonso, E., Pereira-Santaella, M., Fischer, J., et al. 2021, A&A, 645, A49
Gorski, M. D., Aalto, S., König, S., et al. 2023, A&A, 670, A70
Greusard, D., Friedli, D., Wozniak, H., Martinet, L., & Martin, P. 2000, A&AS, 145, 425
Hekatelyne, C., Riffel, R. A., Storchi-Bergmann, T., et al. 2020, MNRAS, 498, 2632
Hickox, R. C., & Alexander, D. M. 2018, ARA&A, 56, 625
Ishibashi, W., Fabian, A. C., & Arakawa, N. 2021, MNRAS, 502, 3638
Lehnert, M. D., Heckman, T. M., & Weaver, K. A. 1999, ApJ, 523, 575
Leroy, A. K., Bolatto, A. D., Ostriker, E. C., et al. 2018, ApJ, 869, 126
Martín, S., Aalto, S., Sakamoto, K., et al. 2016, A&A, 590, A25
Morganti, R., Holt, J., Saripalli, L., Oosterloo, T. A., & Tadhunter, C. N. 2007, A&A, 476, 735
Oya, Y., Sakai, N., Sakai, T., et al. 2014, ApJ, 795, 152
Oya, Y., Watanabe, Y., López-Sepulcre, A., et al. 2021, ApJ, 921, 12
Pereira-Santaella, M., Diamond-Stanic, A. M., Alonso-Herrero, A., & Rieke, G. H. 2010, ApJ, 725, 2270
Pereira-Santaella, M., Alonso-Herrero, A., Santos-Lleo, M., et al. 2011, A&A, 535, A93
Pereira-Santaella, M., Colina, L., García-Burillo, S., et al. 2016, A&A, 594, A81
Pereira-Santaella, M., Colina, L., García-Burillo, S., et al. 2020, A&A, 643, A89
Proga, D. 2007, in The Central Engine of Active Galactic Nuclei, eds. L. C. Ho, & J. W. Wang, ASP Conf. Ser., 373, 267
Pudritz, R. E., & Banerjee, R. 2005, in Massive Star Birth: A Crossroads of Astrophysics, eds. R. Cesaroni, M. Felli, E. Churchwell, & M. Walmsley, 227, 163
Ray, T. P., & Ferreira, J. 2021, New A Rev., 93, 101615a
Roche, P. F., Alonso-Herrero, A., & Gonzalez-Martin, O. 2015, MNRAS, 449, 2598
Roth, N., Kasen, D., Hopkins, P. F., & Quataert, E. 2012, ApJ, 759, 36
Sakai, N., Sakai, T., Hirota, T., et al. 2014, Nature, 507, 78
Sánchez-García, M., Pereira-Santaella, M., García-Burillo, S., et al. 2022, A&A, 659, A102
Sánchez-Monge, Á., Schilke, P., Ginsburg, A., Cesaroni, R., & Schmiedeke, A. 2018, A&A, 609, A101
Sanders, D. B., & Mirabel, I. F. 1996, ARA&A, 34, 749
Sanders, D. B., Mazzarella, J. M., Kim, D. C., Surace, J. A., & Soifer, B. T. 2003, AJ, 126, 1607
Staveley-Smith, L., Norris, R. P., Chapman, J. M., et al. 1992, MNRAS, 258, 725
Takasao, S., Shuto, Y., & Wada, K. 2022, ApJ, 926, 50
Treister, E., Urry, C. M., Schawinski, K., Cardamone, C. N., & Sanders, D. B. 2010, ApJ, 722, L238
van den Broek, A. C., van Driel, W., de Jong, T., et al. 1991, A&AS, 91, 61
Veilleux, S., Shopbell, P. L., & Miller, S. T. 2001, AJ, 121, 198
Veilleux, S., Maiolino, R., Bolatto, A. D., & Aalto, S. 2020, A&A Rev., 28, 2
Vollmer, B., Schartmann, M., Burtscher, L., et al. 2018, A&A, 615, A164
Wada, K. 2012, ApJ, 758, 66
Ziurys, L. M., & Turner, B. E. 1986, ApJ, 300, L19
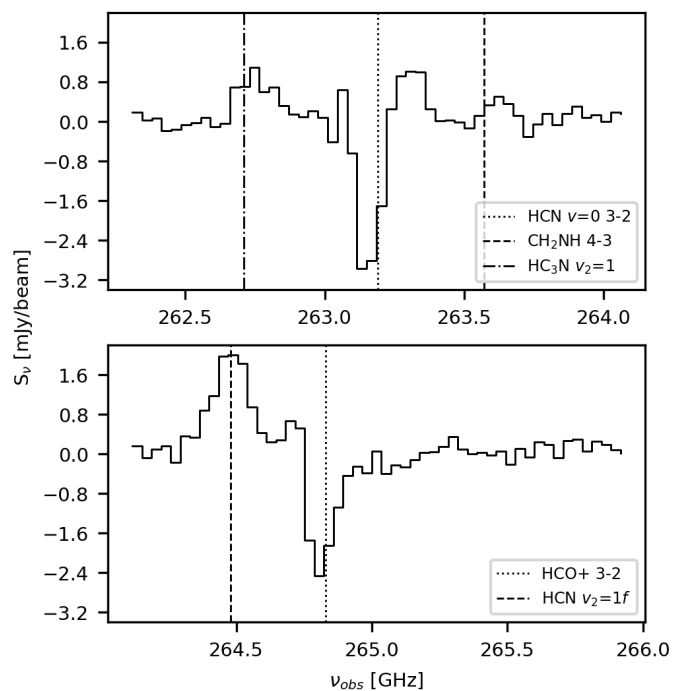
Appendix A: Supplemental plots and figures

Fig. A.1. Spectrum through the peak continuum pixel of two 1.875 GHz wide bands centred at 265.005 GHz and 263.182 GHz with 32 GHz (~40 km s^{-1}) channels. Spectral lines of particular interest are labelled with vertical lines.
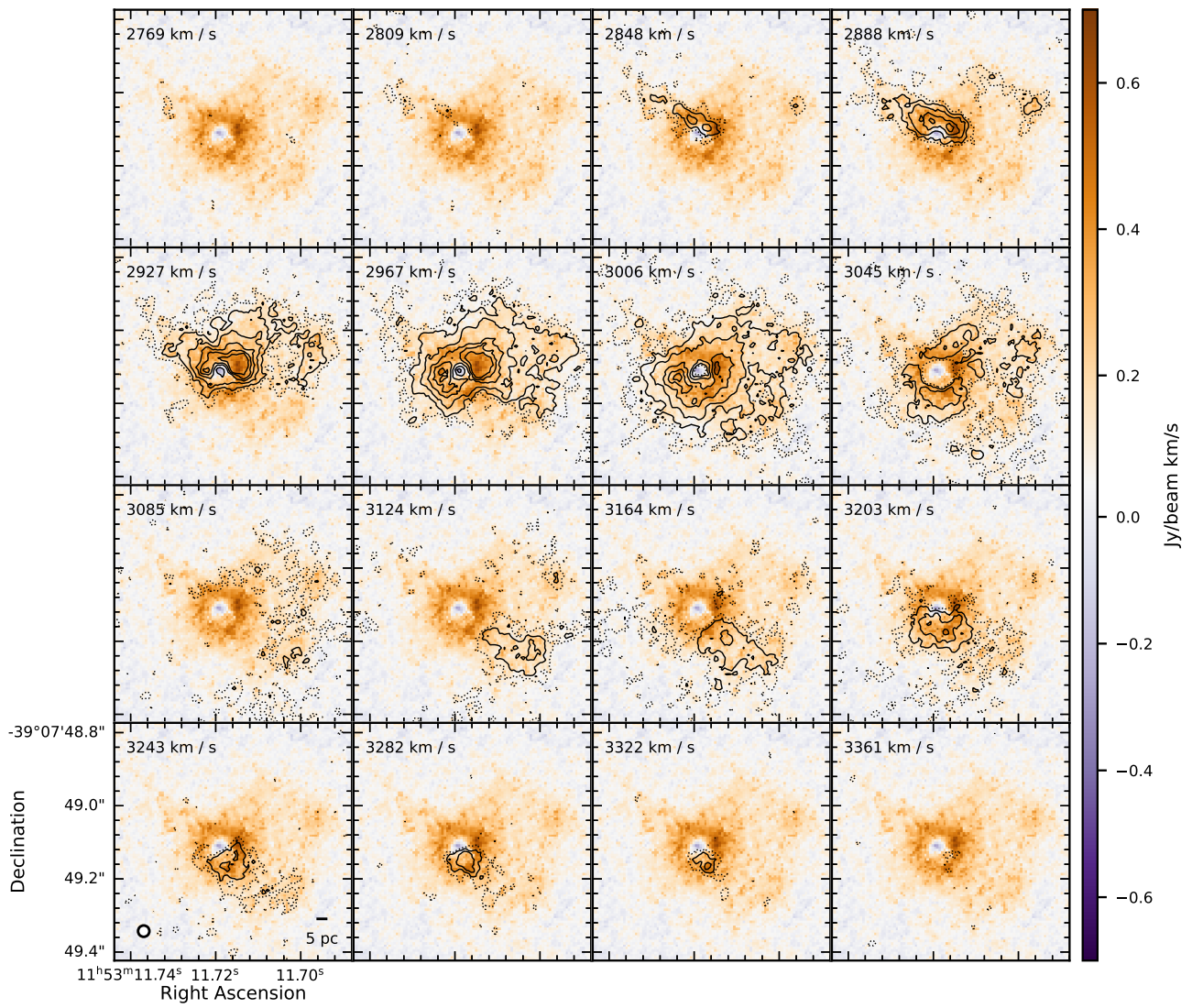
Fig. A.2. Integrated ground-state HCN $v = 0$ $J = 3-2$ emission, and 36 MHz (~ 40 km s^{-1}) wide channel maps with solid contours at 0.14 mJy $\times$ (5, 8, 12,15, and 18). The lowest 0.14 mJy $\times$ 3 contour is dotted.
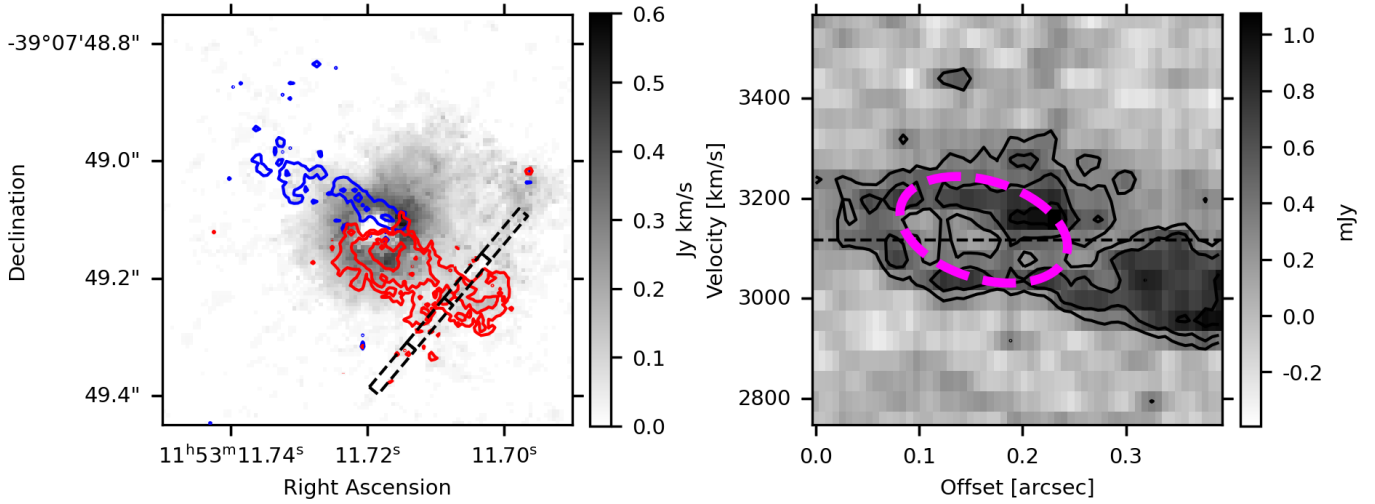
Fig. A.3. [Left] Integrated ground-state HCN $v = 0$ $J = 3-2$ emission (gray scale), with $|v| > 100$ km s^{-1} (with respect to the systemic velocity) contours at $0.015 \times (3, 5, 8,$ and $13)$ Jy km s^{-1}. The blue contours show the approaching outflow, and the red contours show the receding outflow. The dashed black bar indicates the region of the position velocity cut through the redshifted outflow lobe. [Right] Position velocity cut with 0.11 mJy $\times (3, 5,$ and $8)$ contours. The dashed magenta cartoon ellipse shows the characteristic ring of emission indicative of a rotating outflow. The dashed black line shows the systemic velocity of ESO 320-G030.
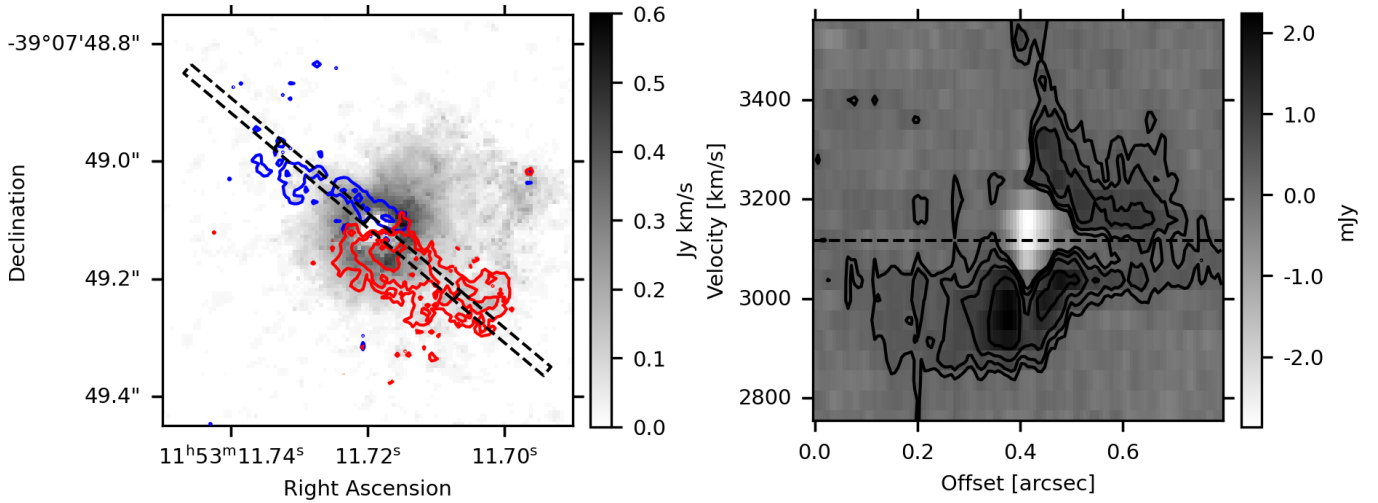

Fig. A.4. [Left] Integrated ground-state HCN $v = 0$ $J = 3-2$ emission (gray scale), with $|v| > 100$ km s^{-1} (with respect to the systemic velocity) contours at $0.015 \times (3, 5, 8,$ and $13)$ Jy km s^{-1}. The blue contours show the approaching outflow, and the red contours show the receding outflow. The dashed black bar indicates the region of the position velocity cut through the redshifted outflow lobe. [Right] Position velocity cut with 0.11 mJy $\times (3, 5,$ and $8)$ contours. The dashed black line shows the systemic velocity of ESO 320-G030.